Three-Dimensional Fe_3O_4@Reduced Graphene Oxide Heterojunctions for High-Performance Room-Temperature NO_2 Sensors

Cheng Zou[1], Jing Hu[2], Yanjie Su[1]*, Feng Shao[1], Zejun Tao[1], Tingting Huo[1], Zhihua Zhou[1], Nantao Hu[1], Zhi Yang[1], Eric Siu-Wai Kong[1] and Yafei Zhang[1]*

[1] Key Laboratory of Thin Film and Microfabrication (Ministry of Education), Department of Micro/Nano Electronics, School of Electronics, Information and Electrical Engineering, Shanghai Jiao Tong University, Shanghai, China, [2] School of Chemistry, Biology and Materials Engineering, Research Center for Nanophotonic and Nanoelectronic Materials, Suzhou University of Science and Technology, Suzhou, China

Metal oxide/reduced graphene oxide (RGO) heterojunctions have been widely used to fabricate room-temperature gas sensors due to large specific surface areas of RGO nanosheets and enhanced carrier separation efficiency at the interface. However, the sheet stacking of RGO nanosheets limits the full utilization of metal oxide/RGO heterojunctions. Herein, we demonstrate a high-performance room-temperature NO_2 gas sensor based on 3D Fe_3O_4@RGO p-n heterojunctions with a core-shell structure, which were synthesized by self-assembly method and further reduction. The effects of different Fe_3O_4/RGO ratios and the relative humidity on the sensing performances have been investigated. The experimental results suggest that the 3D Fe_3O_4@RGO sensor exhibits a good selectivity and high sensitivity of 183.1% for 50 ppm NO_2, which is about 8.17 times higher than that of the pure 2D RGO sensor. When exposed to 50 ppb of NO_2, the response value still reaches 17.8%. This enhanced sensing performance is mainly ascribed to the formed heterojunctions and the larger surface area of RGO nanosheets. This 2D to 3D heterostructure strategy provides a general route to fabricating ultrahigh-performance room-temperature RGO-based gas sensors.

Keywords: Fe_3O_4@RGO heterojuntions, NO_2 sensor, electrostatic self-assembly method, heterostructures, three-dimensional core-shell structure

INTRODUCTION

Toxic gases in the environment pose a severe threat to human health, which has drawn increasing attention in the past few years. Therefore, the detection of toxic gases has become increasingly important (Tyagi et al., 2017; Zhang et al., 2018; Wang et al., 2019a,b). Among common toxic gases, nitrogen dioxide (NO_2) is a corrosive common toxic gas with physiological irritants, which mainly derives from automobile exhaust (Wetchakun et al., 2011). NO_2 is an important factor of the formation of photochemical smog, and it also causes respiratory injury and lung damage to the human body (Kim et al., 2013).

So far, multiple sensors have been presented to monitor NO$_2$ gas (Patil et al., 2016), but the majority of them require operating at high temperatures, have poor sensitivity and contain harmful components. Hence, developing good-performance room-temperature gas sensors based on environmentally friendly materials to detect NO$_2$ is for both human health and environmental protection. Recently, reduced graphene oxide (RGO) has attracted increasing attention in the field of gas sensors due to its regulable functional groups, extremely large specific surface area and good room-temperature conductivity, and it has been used as sensitive materials to detect NO$_2$ at room temperature (Li et al., 2011; Huang et al., 2017a; Hu et al., 2017).

However, 2D RGO generally suffers from agglomeration and overlap during the reduction of GO (Compton and Nguyen, 2010), which may result in a poor sensing performance and long-term response/recovery time under ambient conditions. Recently, more attention has been paid to the 3D RGO (Huang et al., 2017b; Wu et al., 2017). Compared with the traditional 2D RGO, 3D RGO has larger surface areas, which can provide more active sites for adsorbing gas molecules and enhance the sensing performance (Wu et al., 2016).

One the other hand, the sensing performances of pure RGO nanosheets are still suppressed due to the recombination of charged carriers in the RGO channel (Hu et al., 2013; Lipatov et al., 2013). It has been proven that the formation of the heterostructures between RGO and metal oxide semiconductors can accelerate the charge separation at the interface and the transportation process, improving effectively the sensing performance (Zhang et al., 2014; Xia et al., 2016). Moreover, the combination of RGO with metal oxide semiconductors results in a synergistic effect on enhancing the sensing properties of the gas sensors. For example, Zhang et al. (2017) fabricated CuO/rGO isotype heterojunction by a layer-by-layer self-assembly method, which is competent in sub-ppb-level CO gas detection. Wan et al. (2015) synthesized hierarchical In(OH)$_3$ modified graphene p-n heterojunction *via* a microwave-assisted hydrothermal method, which showed enhanced NO$_2$ sensing performances and excellent selectivity. Song et al. (2016) prepared SnO$_2$/rGO nanocomposites by a one-step colloidal synthesis strategy and reported accelerative electron transfer across SnO$_2$/RGO interfaces, which contributed to ultrasensitive H$_2$S gas detection. Among these types of metal oxide/RGO heterojunctions, the 2D heterostructures not only limit the number of adsorption sites for gas molecules but also reduce the interface area between metal oxide and RGO nanosheets, limiting the maximization of the sensing performance.

In this work, a high-performance room-temperature NO$_2$ gas sensor has been demonstrated using unique 3D Fe$_3$O$_4$@RGO core-shell heterostructures, which were synthesized by a self-assembly method and further reduced by ascorbic acid. The effect of different Fe$_3$O$_4$/RGO ratios and the relative humidity on the sensing performances have been investigated. The experimental results show that the 3D Fe$_3$O$_4$@RGO sensor exhibits more prominent sensitivity and selectivity than that of pure RGO, which demonstrates tremendous potential for practical application.

EXPERIMENTAL

Preparation of Modified Fe$_3$O$_4$ Nanospheres

The Fe$_3$O$_4$ nanospheres were synthesized by a hydrothermal method, which has been reported elsewhere (Deng et al., 2005). The as-synthesized Fe$_3$O$_4$ nanospheres were collected and washed by ethanol and water, and then dried at room temperature for further modification. The modification was conducted by adding aminopropyltriethoxysilane (APTES) into the Fe$_3$O$_4$ suspension (Ebrahiminezhad et al., 2013). In a typical procedure, the as-obtained Fe$_3$O$_4$ nanospheres (100 mg) were dissolved in a mixed solution of 15 ml of distilled water and 15 ml of ethanol, followed by the addition of 1 ml of APTES. After stirring for 6 h at an oil bath temperature of 40°C, the as-obtained modified Fe$_3$O$_4$ nanospheres were precipitated magnetically and washed with water and ethanol iteratively to remove redundant APTES.

Preparation of 3D Fe$_3$O$_4$@GO Heterojunctions

Since GO itself is negatively charged and the APTES-modified Fe$_3$O$_4$ nanospheres are positively charged, the 3D Fe$_3$O$_4$@GO heterojunctions with core-shell structure were synthesized by an electrostatic self-assembly method. Firstly, the as-obtained APTES-modified Fe$_3$O$_4$ nanospheres were dispersed in ethanol (10 ml), followed by the addition of 3, 6, 10 and 30 ml of GO suspension (1 mg mL^{-1}), respectively. The mixture was stirred at room temperature for 12 h and the products were collected and washed with ethanol and water repeatedly for later use. The as-obtained products with different mass ratios were denoted as 3wt%-Fe$_3$O$_4$@GO, 6wt%-Fe$_3$O$_4$@GO, 10wt%-Fe$_3$O$_4$@GO, and 30wt%-Fe$_3$O$_4$@GO, respectively.

Fabrication of Fe$_3$O$_4$@RGO Sensors

Firstly, 2 μL of 3D Fe$_3$O$_4$@GO (10 mg/mL) with different mass ratios were dropped onto the interdigital electrodes to obtain a sensing layer, respectively. Afterwards, the electrodes were soaked in 20 mL of 2.5 mg/mL ascorbic acid, to which an appropriate amount of aqueous ammonia was added to make the solution pH≥7. The reduction reaction lasted 6 h in an oil bath at 60°C and was then washed with water and ethanol. The as-obtained devices were denoted as 3wt%-Fe$_3$O$_4$@RGO, 6wt%-Fe$_3$O$_4$@RGO, 10wt%-Fe$_3$O$_4$@RGO, and 30wt%-Fe$_3$O$_4$@RGO, respectively. For comparison, bare RGO without Fe$_3$O$_4$ was prepared by the same reduction process.

Characterization

The morphologies of samples were characterized by a transmission electron microscopy (TEM, Tecnai-G20 of FEI, USA) operating at 200 kV and a field-emission scanning electron microscope (SEM, Ultra 55 of Carl Zeiss, Germany) operating at 5 kV. X-ray diffraction (XRD) tests were used to

characterize the crystallographic structure of the as-synthesized samples at a diffraction angle ranging from 5 to 80° and a scan speed of 3°/min using Bruker D8 ADVANCE (Germany, Cu Kα, λ = 0.154184 nm) X-ray diffractometer. The thermal stability of the samples was measured by a thermogravimetric analyzer (Pyris 1, Perkin-Elmer, USA) under flowing air and with a heating rate of 5°C/min (from 50 to 800°C). Raman spectra were recorded using an inVia Reflex confocal Raman microscope (RENISHAW, England) with a laser wavelength of 633 nm. The X-ray photoelectron spectra (XPS) analysis was acquired using an Escalab 250Xi (Thermo Fisher Scientific) spectrometer with a monochromatic source (Al Kα). The specific surface area was determined by Brunauer-Emmett-Teller (BET) measurement (Micromeritics Tristar 3020, USA).

Gas Sensing Measurement

For the sensing measurement, the sensing device was fixed on a closed test chamber, followed by connection with a dynamic gas mixer system for signal collecting. A semiconductor parameter tester (Agilent 4156C) was used to monitor the sensing signal at a test voltage of 0.5 V. As reported in our previous work (Hu et al., 2017), a homemade gas mixer system was used to obtain different concentrations of NO$_2$ gas, which diluted NO$_2$ standard gas (5,000 ppm) with high-purity dry air. In addition, before testing or during the period of the recovery phase, high-purity dry air was also used for the balance of the adsorption-desorption on the sensing materials surface. Mass flow controllers (MFC, Beijing Qixing Co., Ltd, China) were used to adjust the flow ratio of gases. The NO$_2$ and the air gas mixtures were imported into the testing chamber at a rate of 0.1 L min^{-1} for sensing performance measurement. All the tests were performed at room temperature. The sensing response value (S) is valued by the electrical current change at a test voltage of 0.5 V, which is defined according to the following equation:

$$S\,(\%) = 100\% \times \frac{\Delta I}{I_a} = 100\% \times \frac{I_g - I_a}{I_a} \tag{1}$$

where I_a is the initial electrical current of the sensing device in air, and I_g is the electrical current of the sensing device in the gas mixtures of NO$_2$ and air. Response time and recovery time of the gas sensor are defined as the time which was required to achieve 90% of the total electrical current change.

RESULTS AND DISCUSSION

Microstructure Characterizations

The morphologies of the as-prepared materials were observed by SEM and TEM. **Figure 1a** shows the SEM image of Fe$_3$O$_4$ with a relatively uniform spherical structure. **Figures 1b–f** displays the morphologies of as-prepared Fe$_3$O$_4$@GO with different mass ratios. It can be clearly observed that GO is coated on the Fe$_3$O$_4$ nanospheres, indicating successful preparation of the 3D core-shell structure of GO by the electrostatic self-assembly method. As the mass ratio of GO in Fe$_3$O$_4$@GO increases, the coated GO becomes thicker and more numerous. However, when the GO mass ratio reaches as high as 30%, GO is stacked on the Fe$_3$O$_4$

nanospheres due to the excessive amount of GO, as exhibited in **Figure 1f**. Therefore, a suitable material mass ratio is beneficial to the formation of 3D core-shell structure of Fe$_3$O$_4$@GO. Among them, 10wt%-Fe$_3$O$_4$@GO exhibits a uniform coverage of GO on Fe$_3$O$_4$ nanospheres, as shown in **Figure 1d**. **Figure 1e** shows an enlarged view of the green region in **Figure 1d**, which demonstrates the uniformity of GO coating and the successful fabrication of 3D core-shell structures more intuitively.

Figure 2 shows the SEM and TEM images of 10wt%-Fe$_3$O$_4$@RGO heterojunctions. The morphology of the RGO wrapped on the Fe$_3$O$_4$ nanospheres was maintained after the reduction process by ascorbic acid, indicating that this reduction method did not destroy the 3D core-shell structures of Fe$_3$O$_4$@RGO, as shown in **Figure 2a** (SEM image). TEM images of Fe$_3$O$_4$@RGO are shown in **Figures 2b–d**. The RGO nanosheets cladded on the Fe$_3$O$_4$ nanospheres cannot be observed so expressly because of the lack of electron contrast. However, the RGO junctions between Fe$_3$O$_4$ nanospheres demonstrate the electrostatic self-assembly contact between RGO nanosheets and Fe$_3$O$_4$ nanospheres. An enlarged view of **Figure 2b** is displayed in **Figure 2c**, where it can be clearly seen that RGO nanosheets are tightly attached to the surface of the Fe$_3$O$_4$ nanospheres. The 0.48 nm lattice fringe spacing in **Figure 2d** (HRTEM image) corresponds to the (111) crystal planes of Fe$_3$O$_4$ (Lu et al., 2009a).

XRD patterns and TGA curves of the as-prepared Fe$_3$O$_4$@RGO heterojunctions are illustrated in **Figure 3** to confirm its crystallographic information and chemical composition. For XRD patterns in **Figure 3A**, the diffraction peaks of Fe$_3$O$_4$ are observed at 30.1, 35.4, 43.0, 57.0, and 62.6° which are assigned to the (220), (311), (400), (511), and (440) planes of Fe$_3$O$_4$ (JCPDS card 19-0629), respectively (Sun et al., 2009). The main XRD characteristic peaks for Fe$_3$O$_4$@GO and Fe$_3$O$_4$@RGO can be attributed to the inverse spinel structure of Fe$_3$O$_4$ (JCPDS card 19-0629). This is consistent with the results of TEM. However, the characteristic peaks of GO and RGO disappear in the patterns of the Fe$_3$O$_4$@GO and Fe$_3$O$_4$@RGO due to the relatively low contents.

TGA analysis was carried out to confirm the contents of RGO in the as-prepared Fe$_3$O$_4$@RGO heterojunctions, as exhibited in **Figure 3B**. For the Fe$_3$O$_4$ samples, the weight change can be segmented into three steps. The first stage of weight loss is occurring under 150°C, which is mainly ascribed to desorption of bond water on the surface of material. Subsequently, there is the formation of γ-Fe$_2$O$_3$ due to the oxidation process of Fe$_3$O$_4$ from 150 to 300°C, resulting in an increase in weight (Cao et al., 2008). Finally, the weight loss takes place again from 350–600°C, which can be ascribed to the phase conversion from γ-Fe$_2$O$_3$ to α-Fe$_2$O$_3$ (El Mendili et al., 2012). Notably, for the Fe$_3$O$_4$@RGO heterojunctions, the weight loss continues from about 300°C to about 450°C, which is attributed to the decomposition of RGO (Stankovich et al., 2007). Obviously, during the decomposition of RGO, there is more and more weight loss with the increase of the contents of RGO, indicating the successful preparation of different mass ratio of the Fe$_3$O$_4$@RGO. However, after the reduction process of GO, the weight of the RGO might be
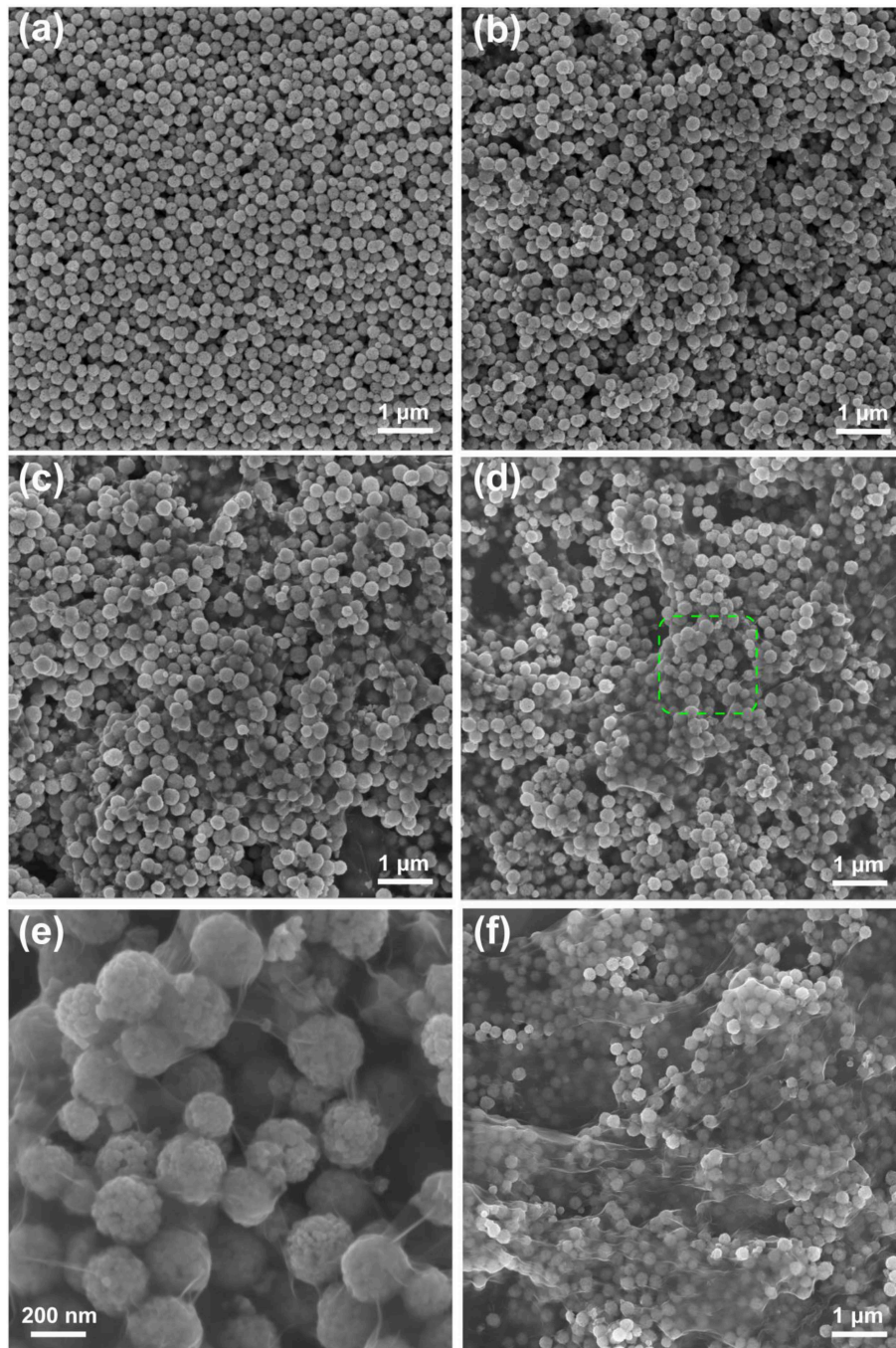
FIGURE 1 | The SEM images of **(a)** pure Fe$_3$O$_4$, **(b)** 3wt%-Fe$_3$O$_4$@GO, **(c)** 6wt%-Fe$_3$O$_4$@GO, **(d)** 10wt%-Fe$_3$O$_4$@GO, **(e)** enlarged view of 10wt%-Fe$_3$O$_4$@GO, **(f)** 30wt%-Fe$_3$O$_4$@GO.

changed, resulting in a change in the mass ratio. For instance, the mass ratio of RGO in the 10wt%-Fe$_3$O$_4$@RGO is ∼5.9% rather than 10%.

To characterize the surface areas of the as-prepared RGO and 10wt%-Fe$_3$O$_4$@RGO, nitrogen adsorption-desorption isotherm analysis was conducted (**Figure S1**). The BET surface area (34.5328 m^2/g) of 10wt%-Fe$_3$O$_4$@RGO is larger than that of

the RGO (2.7045 m^2/g). The bare RGO has undergone heavy agglomeration in a large-scale preparation, resulting in its low BET surface area. In consideration of 10% content GO in Fe$_3$O$_4$@GO samples, the surface area is remarkably enhanced by forming 3D core-shell structures.

Raman spectra research was carried out to analyze graphene and its derivatives. **Figure 4A** shows the Raman spectra of
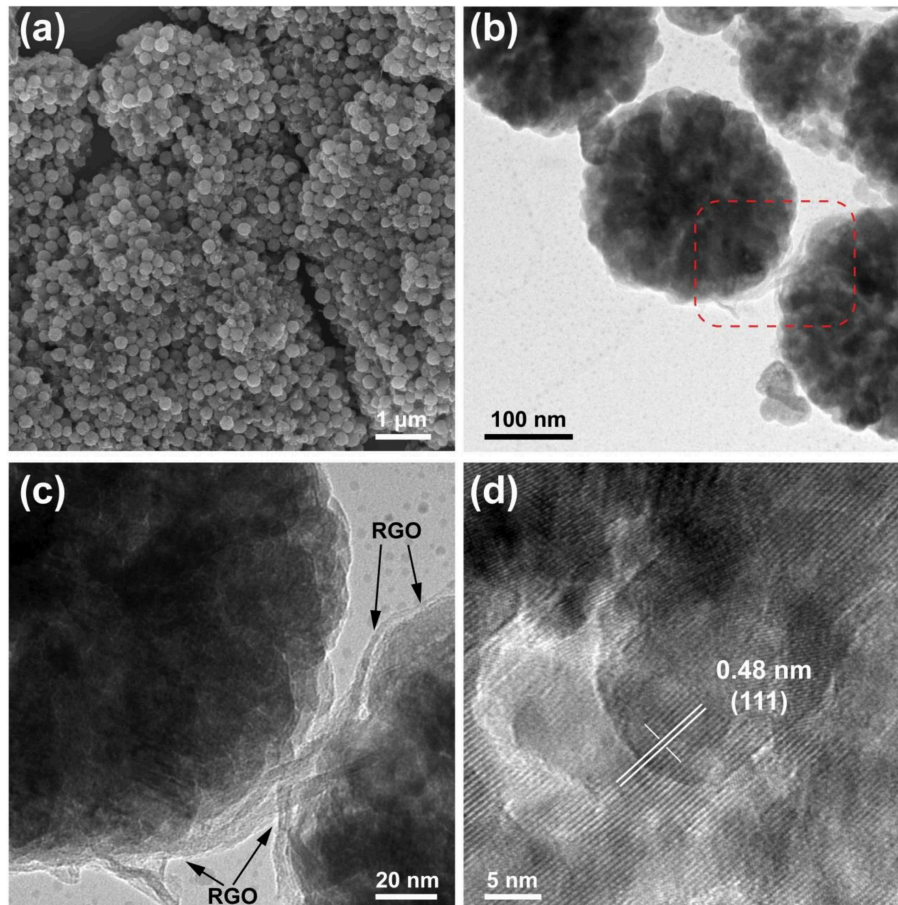
FIGURE 2 | The SEM images of **(a)** 10wt%-Fe$_3$O$_4$@RGO, typical TEM images of **(b)** 10wt%-Fe$_3$O$_4$@RGO, **(c)** enlarged view of 10wt%-Fe$_3$O$_4$@RGO and **(d)** HRTEM image of 10wt%-Fe$_3$O$_4$@RGO.
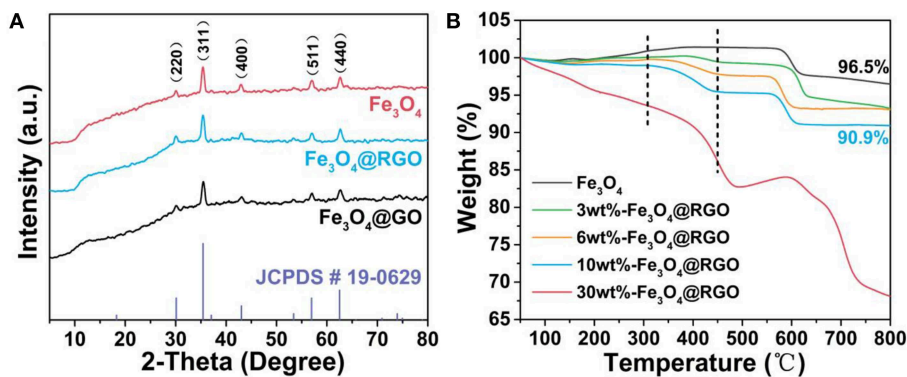
FIGURE 3 | (A) XRD patterns of pure Fe$_3$O$_4$, 10wt%-Fe$_3$O$_4$@GO and 10wt%-Fe$_3$O$_4$@RGO, and the standard patterns of Fe$_3$O$_4$ phase (JCPDS card 19-0629). **(B)** TGA curves of pure Fe$_3$O$_4$ and the different material mass ratio of the Fe$_3$O$_4$@RGO.

Fe$_3$O$_4$@GO, Fe$_3$O$_4$@RGO and RGO. The D and G peaks of graphene are clearly observed in all curves. The peaks at about 660 cm^{-1} of Fe$_3$O$_4$@GO and Fe$_3$O$_4$@RGO can be attributed to the A$_{1g}$ mode of Fe$_3$O$_4$ (Sun et al., 2009). The appearance

of the characteristic peaks of RGO and Fe$_3$O$_4$ indicates the successful modification of RGO on Fe$_3$O$_4$. The D band and G band of Fe$_3$O$_4$@RGO locate at 1324.9 cm^{-1} and 1595.9 cm^{-1}, respectively, while that of RGO locates at 1327.1 cm^{-1} and 1601.1
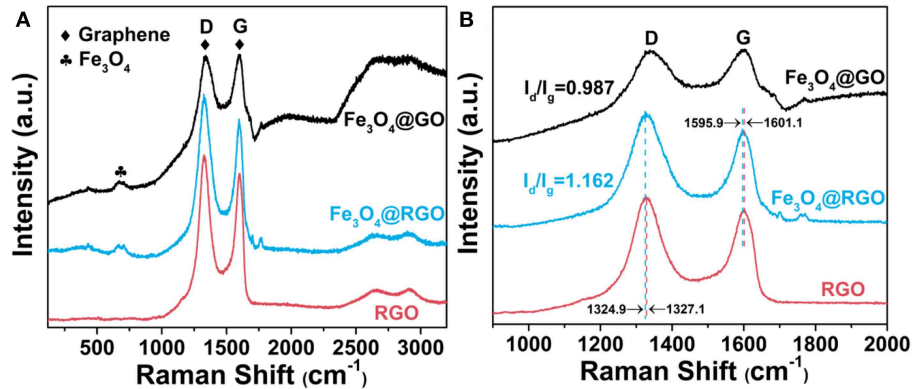
FIGURE 4 | (A) Raman spectra and **(B)** enlarged Raman spectra of RGO, 10wt%-Fe$_3$O$_4$@GO and 10wt%-Fe$_3$O$_4$@RGO.

FIGURE 5 | (A) XPS survey spectra of 10wt%-Fe$_3$O$_4$@GO and 10wt%-Fe$_3$O$_4$@RGO. **(B)** High resolution XPS spectrum of Fe 2p of 10wt%-Fe$_3$O$_4$@RGO. C 1s deconvoluted spectra of **(C)** 10wt%-Fe$_3$O$_4$@GO and **(D)** 10wt%-Fe$_3$O$_4$@RGO.

cm^{-1}, respectively (Liu et al., 2017), as shown in **Figure 4B**. The downshift of several wavenumbers indicates electron transfer from Fe$_3$O$_4$ nanospheres to 3D RGO, as illustrated in the literature (Rao et al., 2014; Hu et al., 2018b). This also confirms the formation of heterostructures between RGO and Fe$_3$O$_4$ in Fe$_3$O$_4$@RGO. In addition, the I$_D$/I$_G$ value of Fe$_3$O$_4$@RGO (1.162) is higher than that of Fe$_3$O$_4$@GO (0.987), implying a decrease in the average size of the sp^2 domain and an increase

in domain numbers during the reduction process (Huang et al., 2017a). This in turn confirms the formation of Fe$_3$O$_4$@RGO by the reduction process of Fe$_3$O$_4$@GO.

The surface structure of Fe$_3$O$_4$@RGO heterojunctions was further investigated by XPS technique. As shown in **Figure 5A**, the survey spectra identify the presence of Fe, C, N, and O elements in the Fe$_3$O$_4$@GO and Fe$_3$O$_4$@RGO. The existence of N 1s can be ascribed to the residual APTES left on the
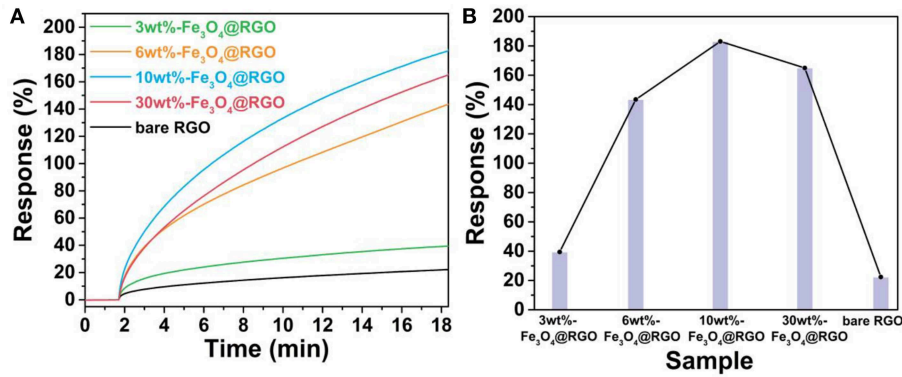
FIGURE 6 | (A) Response curves and **(B)** comparison of response values of RGO and the different material mass ratio of the Fe$_3$O$_4$@RGO toward 50 ppm NO$_2$.
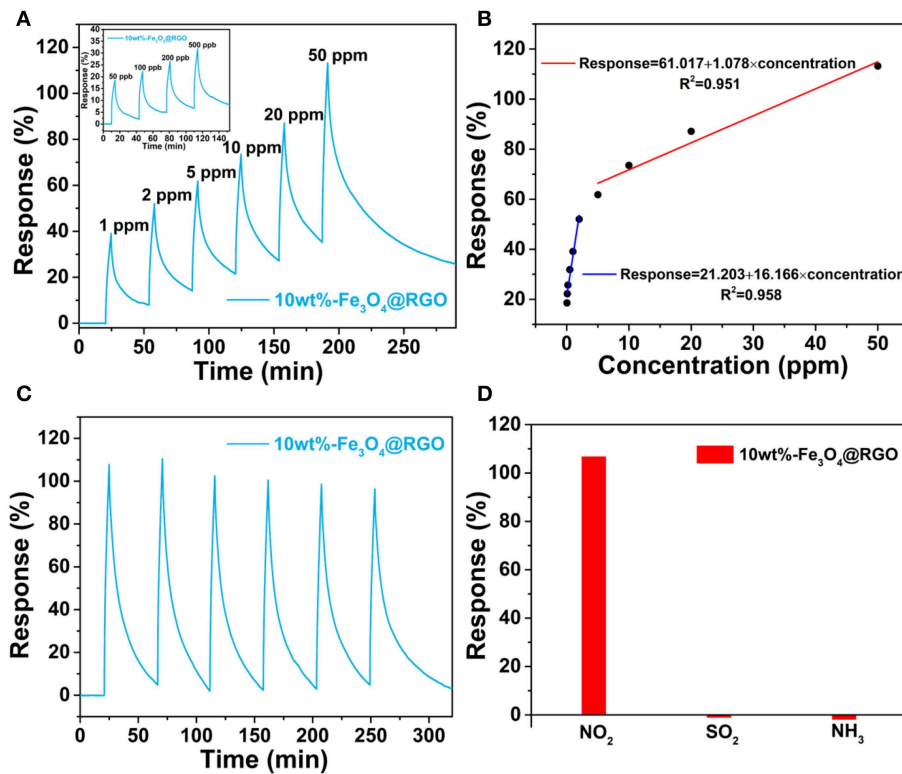

FIGURE 7 | (A) Dynamic curves of 10wt%-Fe$_3$O$_4$@RGO to different NO$_2$ concentrations. **(B)** Response variation of the 10wt%-Fe$_3$O$_4$@RGO sensor as a function of NO$_2$ concentration. **(C)** Six successive sensing cycles of 10wt%-Fe$_3$O$_4$@RGO to 50 ppm NO$_2$. **(D)** Selectivity of the as-fabricated sensor upon exposure to 50 ppm NO$_2$, SO$_2$ and NH$_3$ gas.

surface of Fe$_3$O$_4$ nanospheres. **Figure 5B** shows the Fe core level (Fe 2p) spectra of Fe$_3$O$_4$@RGO. The peaks at 708.6 eV and 716 eV correspond to the main peak and satellite peak of Fe^{2+} 2p$_{3/2}$, respectively. The peaks at around 710.6 eV can be ascribed to the main peak of Fe^{3+} 2p$_{3/2}$, while the peaks at around 724 eV are attributed to the main peak of Fe^{3+} 2p$_{1/2}$. Additionally, the satellite peak of Fe^{3+} 2p$_{3/2}$ appears at ~719 eV. All these results indicate the formation of Fe$_3$O$_4$ (Fujii et al.,

1999). **Figures 5C,D** show the C 1s spectra of Fe$_3$O$_4$@GO and Fe$_3$O$_4$@RGO, these peaks can be grouped into four components: C-C/C=C (~284.6 eV), C-O (~285.8 eV), C=O (~286.8 eV), O-C=O (~288.4 eV) (Zhang et al., 2010; Zheng et al., 2018). It is apparent that the peak of the C=O tremendously decreases and that of C-C/C=C correspondingly increases after the reduction process, which indicates the successful reduction of the GO on the surface of Fe$_3$O$_4$ nanospheres.
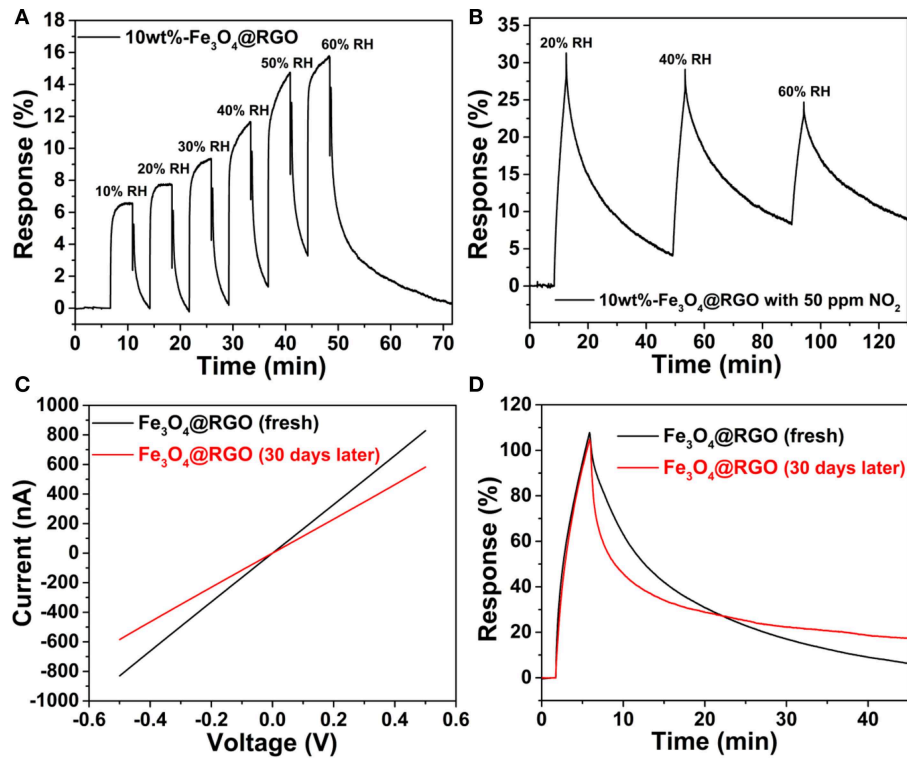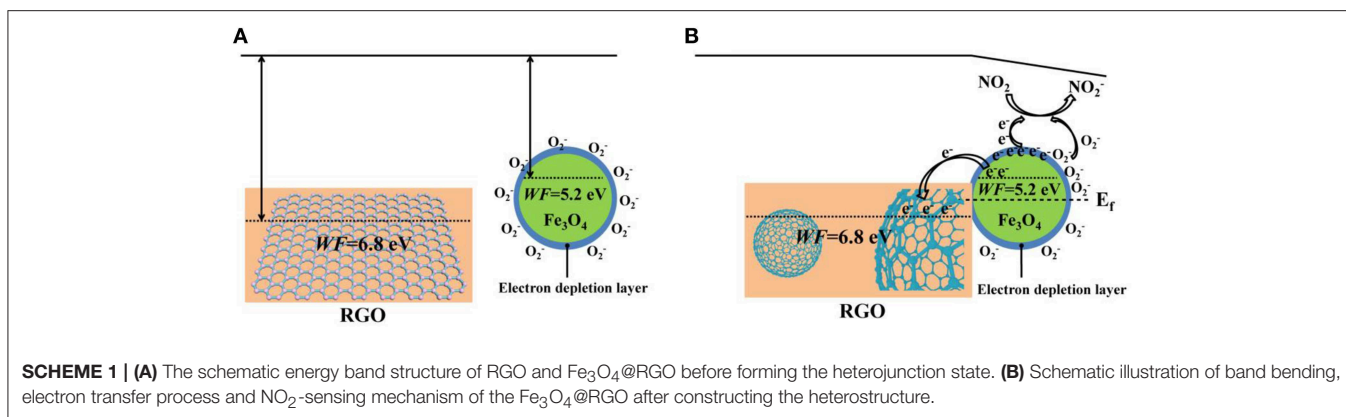
FIGURE 8 | (A) Dynamic curves of 10wt%-Fe$_3$O$_4$@RGO to different relative humidity. **(B)** Response curve for 10wt%-Fe$_3$O$_4$@RGO sensor at different relative humidity for 50 ppm NO$_2$. **(C)** I-V curves and **(D)** response-recovery curves toward 50 ppm NO$_2$ of the fresh 10wt%-Fe$_3$O$_4$@RGO sensor and the sensor after 30 days of storage.

Gas Sensing Properties

The sensing performance of the Fe$_3$O$_4$@RGO heterojunctions was firstly investigated by monitoring their response to NO$_2$ at room temperature. **Figure 6A** shows the single response curves of the devices toward 50 ppm NO$_2$, and **Figure S2** shows the resistance change of 10wt%-Fe$_3$O$_4$@RGO and pure RGO in this response process. When exposed to NO$_2$, the continuous increase of current means that the resistance of the devices continues to decrease, indicating that RGO and Fe$_3$O$_4$@RGO exhibit the p-type semiconductor properties (Lu et al., 2009b). The response value in 1000 s for bare RGO, 3wt%-Fe$_3$O$_4$@RGO, 6wt%-Fe$_3$O$_4$@RGO, 10wt%-Fe$_3$O$_4$@RGO, and 30wt%-Fe$_3$O$_4$@RGO toward 50 ppm NO$_2$ were 22.4, 39.5, 143.5, 183.1, and 165.1%, respectively. The greatly higher performance of Fe$_3$O$_4$@RGO heterojunctions than bare RGO could be ascribed to the optimized structures and the formed heterostructures. As shown in **Figure 6B**, the effect of the amount of RGO on the sensing performances was evaluated. As the amount of RGO increases, the response values increase initially and then decrease. 10wt%-Fe$_3$O$_4$@RGO possesses of the highest response value of 183.1%, which is 8.17 times higher than that of bare RGO. In consideration of the dramatic increases of the electrical current of the as-fabricated sensors in time of the initiatory detection period, an appropriate response time of 250 s was defined for the following tests.

Figure 7A shows the response-recovery curves of the 10wt%-Fe$_3$O$_4$@RGO upon successive exposure to NO$_2$ concentrations ranging from 50 to 500 ppb and from 1 to 50 ppm at room temperature, respectively. It can be seen that the as-fabricated sensor exhibits a prominent response behavior over a wide range of NO$_2$ concentrations. For example, the response value can still reach 17.8% when the as-fabricated sensor is exposed to 50 ppb of NO$_2$, which indicates that the 10wt%-Fe$_3$O$_4$@RGO sensor has an excellent detecting ability toward NO$_2$ with low concentration. It is interesting that the response value is linearly proportional to the concentration of NO$_2$ in two stages, with the first stage being in the range of lower than 2 ppm and the other stage being from 5 to 50 ppm (**Figure 7B**). It is attributed to partial saturation at higher NO$_2$ concentration, which causes the conductance response to diverge from linearity (Hu et al., 2017). The detection ability at lower concentration and the piecewise linear relationship between response values and NO$_2$ concentrations both imply that the 10wt%-Fe$_3$O$_4$@RGO sensor is beneficial for practical application.

To further evaluate the gas-sensing performance of 10wt%-Fe$_3$O$_4$@RGO heterojunctions, the curve of six sequential cycles of the as-fabricated sensor toward 50 ppm NO$_2$ are recorded in **Figure 7C**, demonstrating an excellent reproducibility and cycle stability. Besides high sensitivity and good stability, gas sensors require selectivity for practical applications. From **Figure 7D**,

SCHEME 1 | (A) The schematic energy band structure of RGO and Fe$_3$O$_4$@RGO before forming the heterojunction state. **(B)** Schematic illustration of band bending, electron transfer process and NO$_2$-sensing mechanism of the Fe$_3$O$_4$@RGO after constructing the heterostructure.

it can be found that the 10wt%-Fe$_3$O$_4$@RGO sensor exhibits a prominent selectivity to NO$_2$ gas among NH$_3$, SO$_2$, and NO$_2$. When exposing the as-fabricated sensor to these gases with the same concentration (50 ppm) for 250 s, the 10wt%-Fe$_3$O$_4$@RGO sensor performs a 107% response to NO$_2$, which is ~82 and ~51 times as much as the response to SO$_2$ and NH$_3$, respectively.
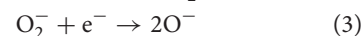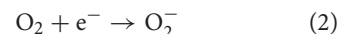
As a crucial factor of sensor properties, the influence of relative humidity (RH) is very important. In this work, the sensor device was exposed to varying levels of humidity, and the influence of humidity on sensing properties was investigated. **Figure 8A** shows the response-recovery curves of the 10wt%-Fe$_3$O$_4$@RGO sensor with different RHs (from 10 to 60% RH) at room temperature. The results suggest that the as-fabricated sensor shows a fast response-recovery to humidity. However, the response value is still low even if the RH reached 60%. Since the NO$_2$ tests were carried out around 40% RH external environment, the as-fabricated sensor was repeatedly exposed to 40% RH. As shown in **Figure S3**, the 10wt%-Fe$_3$O$_4$@RGO sensor exhibited a stable response and fast recovery after six successive cycles, which indicates an excellent repeatability and cycle stability. Besides, rapid recovery means that the adsorbed water molecules can quickly desorb on the surface of the sensing materials. Hence, it can be concluded that humidity in the external environment has an acceptable impact on detecting NO$_2$. That will be favorable for practical tests and providing credible signals. In addition, the effects of different RHs on NO$_2$ detection (50 ppm) of the 10wt%-Fe$_3$O$_4$@RGO sensor at room temperature have also been studied, as shown in **Figure 8B**. The NO$_2$ detection performance of the 10wt%-Fe$_3$O$_4$@RGO sensor gets worse as the RHs increases from 20 to 60%, which can be attributed to the consumption of NO$_2$ molecules due to the reactions between NO$_2$ and water vapor in moist air (Hu et al., 2018a). As the humidity increases, the sensing film is covered by water molecules, which decreases the sensing performance.

Long-term stability is also an important parameter in gas sensing. For the purpose of evaluating the stability of the Fe$_3$O$_4$@RGO gas sensor, the sensing device had been stored under ambient conditions for 1 month for testing. The current-voltage (I-V) curves are shown in **Figure 8C**, which demonstrates that the resistance of the sensing device increased

from 0.602 to 0.856 MΩ. The sensing test results toward 50 ppm NO$_2$ are shown in **Figure 8D**. It is noted that the response of the sensor did not decay after 1 month of storage. The only drawback is that the recovery capability became a little bit weaker, which may be ascribed to the effect of absorbed gas molecules in the air on the surface of the sensing material. In a word, the sensor based on Fe$_3$O$_4$@RGO exhibits an excellent stability.

Gas Sensing Mechanism

The enhancement of the NO$_2$ sensing performances in 3D Fe$_3$O$_4$@RGO can be interpreted by the following aspects. Firstly, a possible surface electron depletion layer mechanism is used to explain the sensing mechanism, as shown in **Scheme 1**. As we know, Fe$_3$O$_4$ is a typical n-type semiconductor (Ai et al., 2010). When exposed to air, oxygen molecules contact the surface of the Fe$_3$O$_4$ and capture electrons from the semiconductor, producing chemisorbed oxygen species (O$^-$, O$_2^-$) and causing a depletion layer on the surface of the Fe$_3$O$_4$ (Wagner et al., 2011; Hu et al., 2018b). Afterwards, when exposed to the oxidizing gases such as NO$_2$, NO$_2$ captures electrons from the surface electron depletion layer of the Fe$_3$O$_4$ and also reacts with O$_2^-$ to form NO$_2^-$; the equations are as follows (Hu et al., 2017, 2018b):

$$O_2 + e^- \rightarrow O_2^- \qquad (2)$$
$$O_2^- + e^- \rightarrow 2O^- \qquad (3)$$
$$NO_2 + e^- \rightarrow NO_2^- \qquad (4)$$
$$NO_2 + O_2^- + 2e^- \rightarrow NO_2^- + 2O^- \qquad (5)$$

The process leads to a decrease in the number of electrons in the semiconductor (n-type), resulting in a decrease in electrical conductivity. On the contrary, for a p-type semiconductor such as RGO and the as-prepared Fe$_3$O$_4$@RGO, since their main carriers are holes rather than electrons, this process leads to an increase in electrical conductivity. When exposed to the reducing gas such as NH$_3$, the electron of the adsorbed electron-donated NH$_3$ is transferred to the p-type Fe$_3$O$_4$@RGO, which reduces the concentration of hole carriers, resulting in a decreased conductivity of the device (Huang et al., 2017b). The good selectivity for NO$_2$ gas can be interpreted as follows: As a small-sized polar molecule with lone pair electrons and

high affinity, NO$_2$ can undergo fierce electron exchange with Fe$_3$O$_4$@RGO (Shaik et al., 2016). Hence, it is very easy for NO$_2$ to capture electrons from p-type Fe$_3$O$_4$@RGO. This results in the formation of a large number of holes, which significantly changes the conductance of the device. Additionally, due to the presence of the Fe$_3$O$_4$@RGO heterojunctions, NO$_2$ can adsorb selectively and react easily with the generated oxygen species (Hu et al., 2017).

The gas-sensing response enhancement brought by the 3D Fe$_3$O$_4$@RGO core-shell structures can be attributed to the well-known p-n heterojunction effect. According to the previous report, RGO has a work function (WF) of 6.8 eV (Kumar et al., 2013), which contains only carboxyl groups and has an oxygen content of 20%. In this work, it can be seen from the results of XPS that the oxygen content in RGO is approximately 27.8%. The work function of Fe$_3$O$_4$ is about 5.2 eV (Fonin et al., 2005), which is lower than that of RGO. When Fe$_3$O$_4$ and RGO are in contact with each other, a p-n junction is formed at the interface of Fe$_3$O$_4$ and RGO, and electrons are transferred from Fe$_3$O$_4$ to RGO until the Fermi level (E$_f$) reaches equilibrium, forming a built-in electric field (space charge region). When the Fe$_3$O$_4$@RGO heterojunctions are exposed to electron-withdrawing NO$_2$, the electron concentration of Fe$_3$O$_4$ is lowered, and a large amount of holes are generated. These holes are rapidly transferred to RGO by the built-in electric field, which further enhances the electrical conductivity of the Fe$_3$O$_4$@RGO. It can be summarized that the formed heterojunctions promote the carrier transfer and further enhance the gas sensing properties (Miller et al., 2014; Song et al., 2016). Meanwhile, the high carrier mobility characteristics of RGO provide smooth and fast channels for carrier transport, which facilitates fast response of the sensor (Li et al., 2011; Feng et al., 2013).

In addition to the p-n junction, the 3D core-shell structure also plays a role in boosting the sensing properties of the Fe$_3$O$_4$@RGO heterojunctions. The 3D Fe$_3$O$_4$@RGO heterostructures prevent agglomeration during the reduction of RGO and can provide more adsorption sites than 2D RGO due to the larger surface area (Song et al., 2016; Huang et al., 2017a). The synergistic effect of Fe$_3$O$_4$ and RGO is also one of the reasons for promoting sensing performances. Therefore, these factors work together to have effects on the electrical properties at the interface of the 3D Fe$_3$O$_4$@RGO heterojunctions, dramatically improving the sensing performance.

CONCLUSION

Unique 3D Fe$_3$O$_4$@RGO core-shell heterostructures have been synthesized by self-assembly and further reduction, which can be used to fabricate high-performance room-temperature NO$_2$ gas sensors. We have investigated the effect of different Fe$_3$O$_4$/RGO ratios and relative humidity on the sensing performances. The sensor based on 3D Fe$_3$O$_4$@RGO p-n heterojunctions exhibits a high sensitivity of 183.1% for 50 ppm NO$_2$ at room temperature, which is about 8.17 times higher than that of the pure 2D RGO sensor. The as-formed heterojunctions and the larger surface area of RGO nanosheets with 3D structures are considered to play a key role in enhancing the sensing performance. We believe that this 2D to 3D core-shell heterostructures strategy enables us to enhance the sensing performance room-temperature RGO-based gas sensors.

DATA AVAILABILITY

All datasets generated for this study are included in the manuscript/**Supplementary Files**.

AUTHOR CONTRIBUTIONS

CZ and YS contributed to all the experimental work. JH and FS analyzed the data. EK and NH contributed to the synthesis of Fe$_3$O$_4$@GO. ZZ and ZT contributed to the synthesis of Fe$_3$O$_4$@RGO. TH and ZY contributed to the characterization of device performance. YS and YZ designed and directed the study. CZ and YS wrote the manuscript. All authors reviewed the paper.

FUNDING

ACKNOWLEDGMENTS

SUPPLEMENTARY MATERIAL

The Supplementary Material for this article can be found online at: https://www.frontiersin.org/articles/10.3389/fmats.2019.00195/full#supplementary-material

REFERENCES

Ai, Z., Deng, K., Wan, Q., Zhang, L., and Lee, S. (2010). Facile microwave-assisted synthesis and magnetic and gas sensing properties of Fe$_3$O$_4$ nanoroses. *J. Phy. Chem. C* 114, 6237–6242. doi: 10.1021/jp910514f

Cao, S.-W., Zhu, Y. J., Ma, M.-Y., Li, L., and Zhang, L. (2008). Hierarchically nanostructured magnetic hollow spheres of Fe$_3$O$_4$ and γ-Fe$_2$O$_3$: preparation and potential application in drug delivery. *J. Phy. Chem. C.* 112, 1851–1856. doi: 10.1021/jp077468+

Compton, O. C., and Nguyen, S. T. (2010). Graphene oxide, highly reduced graphene oxide, and graphene: versatile building blocks for carbon-based materials. *Small* 6, 711–723. doi: 10.1002/smll.200901934

Deng, H., Li, X., Peng, Q., Wang, X., Chen, J., and Li, Y. (2005). Monodisperse magnetic single-crystal ferrite microspheres. *Angew. Chem.* 117, 2842–2845. doi: 10.1002/ange.200462551

Ebrahiminezhad, A., Ghasemi, Y., Rasoul-Amini, S., Barar, J., and Davaran, S. (2013). Preparation of novel magnetic fluorescent nanoparticles using amino acids. *Coll. Surf. B Biointerf.* 102, 534–539. doi: 10.1016/j.colsurfb.2012.08.046

El Mendili, Y., Bardeau, J.-F., Randrianantoandro, N., Grasset, F., and Greneche, J.-M. (2012). Insights into the mechanism related to the phase transition from γ-Fe$_2$O$_3$ to α-Fe$_2$O$_3$ nanoparticles induced by thermal treatment and laser irradiation. *J. Phy. Chem. C* 116, 23785–23792. doi: 10.1021/jp308418x

Feng, H., Cheng, R., Zhao, X., Duan, X., and Li, J. (2013). A low-temperature method to produce highly reduced graphene oxide. *Nat. Commun.* 4:1539. doi: 10.1038/ncomms2848

Fonin, M., Pentcheva, R., Dedkov, Y. S., Sperlich, M., Vyalikh, D. V., Scheffler, M., et al. (2005). Surface electronic structure of the Fe$_3$O$_4$ (100): Evidence of a half-metal to metal transition. *Phys. Rev. B* 72:104436. doi: 10.1103/PhysRevB.72.104436

Fujii, T., de Groot, F. M. F., Sawatzky, G. A., Voogt, F. C., Hibma, T., and Okada, K. (1999). *In situ* XPS analysis of various iron oxide films grown by NO$_2$-assisted molecular-beam epitaxy, *Phy. Rev. B* 59, 3195–3202. doi: 10.1103/PhysRevB.59.3195

Hu, J., Zou, C., Su, Y., Li, M., Han, Y., Kong, E. S.-W., et al. (2018a). An ultrasensitive NO$_2$ gas sensor based on a hierarchical Cu$_2$O/CuO mesocrystal nanoflower. *J. Mater. Chem. A* 6, 17120–17131. doi: 10.1039/C8TA04404J

Hu, J., Zou, C., Su, Y., Li, M., Hu, N., Ni, H., et al. (2017). Enhanced NO$_2$ sensing performance of reduced graphene oxide by *in situ* anchoring carbon dots. *J. Mater. Chem. C* 5, 6862–6871. doi: 10.1039/C7TC01208J

Hu, J., Zou, C., Su, Y., Li, M., Ye, X., Cai, B., et al. (2018b). Light-assisted recovery for a highly-sensitive NO$_2$ sensor based on RGO-CeO$_2$ hybrids. *Sens Actuat. B Chem.* 270, 119–129. doi: 10.1016/j.snb.2018.05.027

Hu, N., Yang, Z., Wang, Y., Zhang, L., Wang, Y., Huang, X., et al. (2013). Ultrafast and sensitive room temperature NH$_3$ gas sensors based on chemically reduced graphene oxide, *Nanotechnology* 25:025502. doi: 10.1088/0957-4484/25/2/025502

Huang, D., Li, X., Wang, S., He, G., Jiang, W., Hu, J., et al. (2017a). Three-dimensional chemically reduced graphene oxide templated by silica spheres for ammonia sensing. *Sens. Actuat. B Chem.* 252, 956–964. doi: 10.1016/j.snb.2017.05.117

Huang, D., Yang, Z., Li, X., Zhang, L., Hu, J., Su, Y., et al. (2017b). Three-dimensional conductive networks based on stacked SiO$_2$@graphene frameworks for enhanced gas sensing, *Nanoscale* 9, 109–118. doi: 10.1039/C6NR06465E

Kim, K.-H., Jahan, S. A., and Kabir, E. (2013). A review on human health perspective of air pollution with respect to allergies and asthma. *Environ. Int.* 59, 41–52. doi: 10.1016/j.envint.2013.05.007

Kumar, P. V., Bernardi, M., and Grossman, J. C. (2013). The impact of functionalization on the stability, work function, and photoluminescence of reduced graphene oxide. *ACS Nano* 7, 1638–1645. doi: 10.1021/nn305507p

Li, W., Geng, X., Guo, Y., Rong, J., Gong, Y., Wu, L., et al. (2011). Reduced graphene oxide electrically contacted graphene sensor for highly sensitive nitric oxide detection. *ACS Nano* 5, 6955–6961. doi: 10.1021/nn201433r

Lipatov, A., Varezhnikov, A., Wilson, P., Sysoev, V., Kolmakov, A., and Sinitskii, A. (2013). Highly selective gas sensor arrays based on thermally reduced graphene oxide. *Nanoscale* 5, 5426–5434. doi: 10.1039/c3nr00747b

Liu, J., Zhao, Y., Z., Li, X., Wang, C., Zeng, Y., Yue, G., et al. (2017). CuCr$_2$O$_4$@rGO nanocomposites as high-performance cathode catalyst for rechargeable lithium-oxygen batteries. *Nano-Micro Lett.* 10:22. doi: 10.1007/s40820-017-0175-z

Lu, G., Ocola, L. E., and Chen, J. (2009b). Gas detection using low-temperature reduced graphene oxide sheets. *Appl. Phys. Lett.* 94, 083111. doi: 10.1063/1.3086896

Lu, J., Jiao, X., Chen, D., and Li, W. (2009a). Solvothermal synthesis and characterization of Fe$_3$O$_4$ and γ-Fe$_2$O$_3$ nanoplates. *J. Phy. Chem. C* 113, 4012–4017. doi: 10.1021/jp810583e

Miller, D. R., Akbar, S. A., and Morris, P. A. (2014). Nanoscale metal oxide-based heterojunctions for gas sensing: a review. *Sens. Actuat. B Chem.* 204, 250–272. doi: 10.1016/j.snb.2014.07.074

Patil, V. L., Vanalakar, S. A., Kamble, A. S., Shendage, S. S., Kim, J. H., and Patil, P. S. (2016). Farming of maize-like zinc oxide via a modified SILAR technique as a selective and sensitive nitrogen dioxide gas sensor. *RSC Adv.* 6, 90916–90922. doi: 10.1039/C6RA06346B

Rao, R., Pierce, N., and Dasgupta, A. (2014). On the charge transfer between single-walled carbon nanotubes and graphene. *Appl. Phys. Lett.* 105:073115. doi: 10.1063/1.4893698

Shaik, M., Rao, V. K., Gupta, M., Murthy, K. S. R. C., and Jain, R. (2016). Chemiresistive gas sensor for the sensitive detection of nitrogen dioxide based on nitrogen doped graphene nanosheets. *RSC Adv.* 6, 1527–1534. doi: 10.1039/C5RA21184K

Song, Z., Wei, Z., Wang, B., Luo, Z., Xu, S., Zhang, W., et al. (2016). Sensitive room-temperature H$_2$S gas sensors employing SnO$_2$ quantum wire/reduced graphene oxide nanocomposites. *Chem. Mater.* 28, 1205–1212. doi: 10.1021/acs.chemmater.5b04850

Stankovich, S., Dikin, D. A., Piner, R. D., Kohlhaas, K. A., Kleinhammes, A., Jia, Y., et al. (2007). Synthesis of graphene-based nanosheets via chemical reduction of exfoliated graphite oxide. *Carbon* 45, 1558–1565. doi: 10.1016/j.carbon.2007.02.034

Sun, X., Zheng, C., Zhang, F., Yang, Y., Wu, G., Yu, A., et al. (2009). Size-controlled synthesis of magnetite (Fe$_3$O$_4$) nanoparticles coated with glucose and gluconic acid from a single Fe(III) precursor by a sucrose bifunctional hydrothermal method. *J. Phy. Chem. C.* 113, 16002–16008. doi: 10.1021/jp9038682

Tyagi, P., Sharma, A., Tomar, M., and Gupta, V. (2017). A comparative study of RGO-SnO$_2$ and MWCNT-SnO$_2$ nanocomposites based SO$_2$ gas sensors. *Sens. Actuators B Chem.* 248, 980–986. doi: 10.1016/j.snb.2017.02.147

Wagner, T., Hennemann, J., Kohl, C. D., and Tiemann, M. (2011). Photocatalytic ozone sensor based on mesoporous indium oxide: Influence of the relative humidity on the sensing performance. *Thin Solid Films* 520, 918–921. doi: 10.1016/j.tsf.2011.04.181

Wan, P., Yang, W., Wang, X., Hu, J., and Zhang, H. (2015). Reduced graphene oxide modified with hierarchical flower-like In(OH)$_3$ for NO$_2$ room-temperature sensing. *Sens. Actuat. B Chem.* 214, 36–42. doi: 10.1016/j.snb.2015.02.100

Wang, K., Li, J., Li, W., Wei, W., Zhang, H., and Wang, L. (2019b). Highly active Co-based catalyst in nanofiber matrix as advanced sensing layer for high selectivity of flexible sensing device. *Adv. Mater. Technol.* 4:1800521. doi: 10.1002/admt.201800521

Wang, L., Chen, S., Li, W., Wang, K., Lou, Z., and Shen, G. (2019a). Grain-boundary-induced drastic sensing performance enhancement of polycrystalline-microwire printed gas sensors. *Adv. Mater.* 31:1804583. doi: 10.1002/adma.201804583

Wetchakun, K., Samerjai, T., Tamaekong, N., Liewhiran, C., Siriwong, C., Kruefu, V., et al. (2011). Semiconducting metal oxides as sensors for environmentally hazardous gases. *Sens Actuat. B Chem.* 160, 580–591. doi: 10.1016/j.snb.2011.08.032

Wu, J., Tao, K., Guo, Y., Li, Z., Wang, X., Luo, Z., et al. (2017). A 3D chemically modified graphene hydrogel for fast, highly sensitive, and selective gas sensor. *Adv. Sci.* 4:1600319. doi: 10.1002/advs.201600319

Wu, J., Tao, K., Zhang, J., Guo, Y., Miao, J., and Norford, L. K. (2016). Chemically functionalized 3D graphene hydrogel for high performance gas sensing. *J. Mater. Chem. A.* 4, 8130–8140. doi: 10.1039/C6TA01426G

Xia, Y., Wang, J., Xu, J.-L., Li, X., Xie, D., Xiang, L., et al. (2016). Confined formation of ultrathin ZnO nanorods/reduced graphene oxide mesoporous nanocomposites for high-performance room-temperature NO$_2$ sensors. *ACS Appl. Mater. Inter.* 8, 35454–35463. doi: 10.1021/acsami.6b12501

Zhang, D., Jiang, C., Liu, J., and Cao, Y. (2017). Carbon monoxide gas sensing at room temperature using copper oxide-decorated graphene hybrid nanocomposite prepared by layer-by-layer self-assembly. *Sens. Actuat. B Chem.* 247, 875–882. doi: 10.1016/j.snb.2017.03.108

Zhang, H., Feng, J., Fei, T., Liu, S., and Zhang, T. (2014). SnO$_2$ nanoparticles-reduced graphene oxide nanocomposites for NO$_2$ sensing at low operating temperature. *Sens. Actuat. B Chem.* 190, 472–478. doi: 10.1016/j.snb.2013.08.067

Zhang, J., Yang, H., Shen, G., Cheng, P., Zhang, J., and Guo, S. (2010). Reduction of graphene oxide vial-ascorbic acid. *Chem. Commun.* 46, 1112–1114. doi: 10.1039/B917705A

Zhang, Z., Haq, M., Wen, Z., Ye, Z., and Zhu, L. (2018). Ultrasensitive ppb-level NO$_2$ gas sensor based on WO$_3$ hollow nanosphers doped with Fe. *Appl. Surf. Sci.* 434, 891–897. doi: 10.1016/j.apsusc.2017.10.074

Zheng, S., Zheng, L., Zhu, Z., Chen, J., Kang, J., Huang, Z., et al. (2018). MoS$_2$ nanosheets arrays rooted on hollow rGO spheres as bifunctional hydrogen evolution catalyst and supercapacitor electrode. *Nano-Micro Lett.* 10:62. doi: 10.1007/s40820-018-0215-3